Journal of
Materials Chemistry A

Materials for energy and sustainability

Accepted Manuscript

This article can be cited before page numbers have been issued, to do this please use: W. Alnoush, N. Noor, S. Angizi, A. Rakhsha, T. Baker and D. Higgins, *J. Mater. Chem. A*, 2026, DOI: 10.1039/D6TA01057A.

ROYAL SOCIETY OF CHEMISTRY

rsc.li/materials-a

View Article Online
DOI: 10.1039/D6TA01057A

Defective Ceria as a Structural and Electronic Modifier of Nitrogen-Doped Carbon and Cobalt-Nitrogen-Carbon Electrocatalysts for Oxygen Reduction in Alkaline Electrolyte

Wajdi Alnoush, Navid Noor, Shayan Angizi, Amirhossein Raksha, Thomas Baker, and Drew Higgins*

Wajdi Alnoush, Chemical Engineering Department, McMaster University
1280 Main St W, Hamilton, ON L8S 4L8, Canada.
alnoushw@mcmaster.ca

Navid Noor, Chemical Engineering Department, McMaster University
1280 Main St W, Hamilton, ON L8S 4L8, Canada.
noormohn@mcmaster.ca

Shayan Angizi, Chemical Engineering Department, McMaster University
1280 Main St W, Hamilton, ON, L8S 4L8, Canada.
angizis@mcmaster.ca

Amirhossein Raksha, Chemical Engineering Department, McMaster University
1280 Main St W, Hamilton, ON, L8S 4L8, Canada.
rakhsha@mcmaster.ca

Thomas Baker, Chemical Engineering Department, McMaster University
1280 Main St W, Hamilton, ON, L8S 4L8, Canada.
bakert4@mcmaster.ca

*Drew Higgins, Chemical Engineering Department, McMaster University
1280 Main St W, Hamilton, ON, L8S 4L8, Canada.
higgid2@mcmaster.ca

Keywords

Electrocatalyst, Oxygen reduction reaction, Cerium oxide, Zeolitic Imidazolate Framework, Oxygen vacancy

View Article Online
DOI: 10.1039/D6TA01057A

Defective Ceria as a Structural and Electronic Modifier of Nitrogen-Doped Carbon and Cobalt-Nitrogen-Carbon Electrocatalysts for Oxygen Reduction in Alkaline Electrolyte

Wajdi Alnoush[1], Navid Noor[1], Shayan Angizi[1], Amirhossein Rakhsha[1], Thomas Baker[1], and Drew Higgins[1]

[1] *Department of Chemical Engineering, McMaster University, Hamilton, ON and L8S 4L8, Canada*

ABSTRACT

The oxygen reduction reaction (ORR) is central to many sustainable energy technologies such as fuel cells, metal-air batteries, and peroxide electrosynthesis, but the scalability of ORR-based technologies requires cost-effective, active, and selective electrocatalysts free from the costly and scarce platinum-group-metals (PGMs). Despite considerable advances, state-of-the-art PGM-free N-doped carbon (N-C) and metal-nitrogen-carbon (M-N_x/C) electrocatalysts face performance bottlenecks. Defect engineering in ceria (CeO_2), a promising electrocatalyst modifier, leveraging its Ce^{3+}/Ce^{4+} redox and oxygen-vacancy (V_o) capacity, offers a promising route to modulate the electronic structure of N-C and M-N_x/C electrocatalysts. However, how V_o in ceria modulate the electronic structure and the $2e^-/4e^-$ ORR selectivity of N-C and Co/N-C electrocatalysts remains underexplored. Here, we engineer V_o-rich ceria via plasma and thermal reduction, followed by embedding into zeolitic imidazolate frameworks (Zn-ZIF8 and Co/Zn-ZIF) and pyrolysis (900 °C) to derive ceria@N-C and ceria@Co/N-C electrocatalysts. The structural and physicochemical properties of the ceria variants, ceria@ZIF precursors, and developed electrocatalyst were investigated. The electrochemical properties and ORR performance were evaluated in alkaline media (0.1 M KOH). V_o-rich ceria samples exhibited enhanced onset and half-wave potentials relative to as-synthesized ceria, while modulating the $2e^-$ and $4e^-$ ORR selectivity differently depending on the host matrix and surrounding type of active site structure(s). In Co-free systems, Ce^{3+}-V_o centers led to mixed $2e^-/4e^-$ pathways, while in Co-containing systems, V_o-rich ceria partially suppressed the dominant $4e^-$ ORR of Co nanoparticles. ECSA-normalized activity confirmed that V_o-rich ceria modulates selectivity but dilutes intrinsic site activity, revealing a trade-off between activity and selectivity. This work establishes V_o defect engineering in ceria as a lever in modulating ZIF-derived ORR electrocatalysts as a strategy toward the rational design of application-ready PGM-free electrocatalysts.

1 Introduction

The devastating environmental impacts of greenhouse gas (GHG) emissions stimulates the development of new climate technologies to sustainably meet global demands for energy and value-added chemicals without fossil fuels. The electrochemical conversion of O_2, an earth-abundant molecule, via the oxygen reduction reaction (ORR) is central to several emerging climate technologies, including proton exchange membrane (PEM) fuel cells [1-4], metal-air batteries [5-7], and green peroxide electrosynthesis [8-10]. These ORR-based technologies operate via one of two primary pathways: i. the $4e^-$ reduction of O_2 to H_2O in acidic media (or OH^- in alkaline media), central to fuel cells and metal-air batteries, or the $2e^-$ reduction of O_2 to H_2O_2 (acidic) or HO_2^- (alkaline), key in peroxide electrosynthesis. Harnessing either pathway demands active, selective, and durable electrocatalysts. To date, commercialized ORR-based technologies still rely heavily on costly and scarce platinum group metals (PGMs), limiting their scalability and globalized adoption. Despite substantial advances in developing PGM-free alternatives, with zeolitic imidazolate framework (ZIF)-derived N-doped carbon (N-C) and atomically dispersed metal-nitrogen-carbon (M-N_x/C) catalysts emerging as leading contenders, critical challenges remain under application-relevant conditions.

In PEM fuel cells, a key challenge is suppressing H_2O_2 formation and free radical (i.e., ·O, ·OH, or ·OOH) attack, which can degrade the membrane and affect long-term durability.[11-14] Inhibiting H_2O_2 formation is also crucial in metal-air batteries to prevent cathode and electrolyte degradation, while battery rechargeability demands bifunctional cathodes able to facilitate both oxygen reduction and evolution reactions.[15] In contrast, green peroxide electrosynthesis demands enhanced selectivity towards H_2O_2/HO_2^-, yet efficient production remains a challenge across the pH scale since peroxides are prone to decomposition in alkaline media, acidic environments degrade most non-noble metal catalysts, and neutral conditions lead to poor activity-selectivity balance.[16, 17] Overcoming these technology-specific bottlenecks has motivated the exploration of rare-earth metals and their oxides as modifiers to fine-tune the selectivity and functionality of PGM-free ORR electrocatalysts.[18-26] Among rare-earth oxides, ceria (CeO_2) has garnered increasing attention as a multifunctional modifier capable of addressing multiple ORR-technology challenges through its ability to scavenge free radicals[27-30], enhance corrosion resistance[31, 32], promote peroxide electrogeneration[33-35], and facilitate bifunctionality by enabling OER[36, 37]. The functional versatility and growing adoption of CeO_2 in ORR electrocatalysts stem from its unique Ce^{3+}/Ce^{4+} redox interconversion, oxygen mobility, and the abundance of Ce amongst other rare-earth metals.[38, 39] Furthermore, oxygen vacancies (V_o) in CeO_2 play a pivotal role in modulating the local electronic structure by inducing electron depletion near Ce atoms and accumulation near O atoms, thereby promoting charge

Address correspondence to Drew Higgins, higgid2@mcmaster.ca

transfer and enhancing catalytic performance. The accelerated charge transfer and superior activity of V_o-rich CeO_2 electrocatalysts compared to V_o-poor CeO_2 have been corroborated by experimental and computational studies.[32, 40, 41] Beyond its intrinsic electronic effects, CeO_2 also exhibits synergistic interfacial interactions with carbonaceous supports[42, 43] and transition metals[44-47] in the form of interfacial charge redistribution and modified adsorption energetics of oxygenated intermediates.

Building on the unique electronic and defect-related properties of ceria, recent studies have incorporated ceria into N-C and M-N_x/C ORR electrocatalysts, leveraging synergistic electronic and interfacial effects to promote charge transfer, stabilize active sites, and improve catalytic performance. For instance, Yu et al.[48] embedded CeO_2 into the cavities of a Zn-ZIF8 precursor. Subsequent pyrolysis yielded CeO_2@N-C materials that demonstrated ORR activity comparable to Pt/C in alkaline media, but with superior stability and methanol-crossover tolerance to Pt/C. Kang et al.[49] encapsulated 3D rose-like CeO_2 in N-doped carbon, followed by pyrolysis to obtain CeO_2@NC-900 electrocatalyst, which exhibited superior ORR activity ($E_{1/2}$ = 0.85 V vs. RHE) and durability (93.4% retention after 50,000 cycles) compared to CeO_2-free NC-900. The electrocatalyst further enabled bifunctionality, delivering OER activity (413 mV overpotential at 10 mA/cm^2) and improved Zn-air battery energy efficiency. Hao et al.[50] introduced CeO_2 and Fe_3O_4 to modify a Zn-ZIF8-derived Fe-N/C electrocatalyst. The resulting CeO_2-Fe_3O_4@Fe-N/C hybrid outperformed CeO_2-free Fe_3O_4@Fe-N/C and Pt/C in both ORR activity ($E_{1/2}$ = 0.89 V vs. RHE) and stability (4 mV loss after 5,000 cycles) in alkaline media. Sivanantham et al.[36] utilized electrospinning to anchor CeO_2-supported Co on N-doped carbon nanorods, followed by pyrolysis to produce a bifunctional ORR/OER electrocatalyst (Co-CeO_2/N-CNR). The electrocatalyst exhibited excellent ORR activity ($E_{1/2}$ = 0.84 V vs. RHE and mass activity of 49.4 A g^{-1}), outperforming CeO_2-free Co/N-CNR and Pt/C, while also enhancing OER, attributed to the synergistic effects between Co and CeO_2. Wang et al.[51] employed density functional theory to screen ten rare-earth metal oxides as modifiers for Co-N-C ORR electrocatalysts, identifying CeO_2 as an optimal promoter that enhances electron transfer and modulates the binding energy of oxygen-containing intermediates via charge regulation. A CeO_2-Co-N-C catalyst was then prepared via pyrolysis. The CeO_2-modified electrocatalyst exhibited excellent ORR activity ($E_{1/2}$ = 0.90 V vs. RHE) and stability (8 mV loss after 10,000 cycles) in alkaline media.

While the potential of ceria-modified N-C and M-N_x/C ORR electrocatalysts has been demonstrated, important gaps remain underexplored. In particular, prior studies emphasize overall performance enhancements without disentangling how defect chemistry in ceria governs the balance between 4e$^-$ and 2e$^-$ ORR pathways or interfacial charge transfer. Moreover, how different V_o generation methods influence defect distribution and subsequent ceria-support synergy modulate N-C and metallic nanoparticle-containing Co/N-C catalysts remains poorly understood.

To unravel the relationships among V_o-formation, defect distribution, ceria-support interactions, and the impact on ORR activity and selectivity, we systematically engineered defective ceria as modifiers to ZIF-derived N-C and Co/N-C electrocatalysts. First, fluorite ceria (CeO_2) was synthesized and then treated to induce V_o-generation via two methods: reduction under air plasma, yielding plasma-reduced ceria (prCeO_2), and thermal treatment at 400 °C under a reducing environment (3% H_2 in N_2), yielding thermally-reduced ceria (trCeO_2). These ceria variants were embedded within Zn-ZIF8 and Co/Zn-ZIF to form ceria@Zn-ZIF8 and ceria@Co/Zn-ZIF precursors, followed by pyrolysis at 900 °C to derive ceria@N-C and ceria@Co/N-C electrocatalysts (Scheme 1). The structural and physiochemical properties of the ceria variants, ceria@ZIF precursors, and developed electrocatalysts were characterized with X-ray diffraction, electron paramagnetic resonance, Raman spectroscopy, thermogravimetric analysis, and scanning and transmission electron microscopy. The ORR performance was evaluated using the rotating ring-disk electrode (RRDE) technique in 0.1 M KOH.

We demonstrate that the concentration and distribution of V_o in ceria impact electronic structure, electrochemical properties, and ORR pathway selectivity of ceria@N-C and ceria@Co/N-C electrocatalysts. Plasma treatment was found to induce surface-concentrated defects while thermal reduction yielded bulk-distributed defects in the ceria. A high concentration of V_o in ceria was found to act as an electronic modulator that enhances the ORR activity of ceria@N-C and ceria@Co/N-C electrocatalysts, with the selectivity toward the 2e$^-$ or 4e$^-$ ORR pathway being dependent on the type of active site structure(s) present in the catalyst. Peroxide quantification and stability measurements corroborate that defective ceria can regulate the formation, stabilization, and release of HO_2^-, thus modulating ORR selectivity without negatively impacting durability. Overall, ceria defect-engineering provides a versatile strategy to modulate the activity and selectivity of PGM-free ZIF-derived ORR electrocatalysts.

2 Results and Discussion

2.1 Defect generation and precursor characterization

To confirm the successful synthesis of fluorite CeO_2 via thermal decomposition of cerium(III) acetate, assess phase purity, and probe crystallinity changes induced by plasma and thermal reduction, we examined CeO_2, prCeO_2, and trCeO_2 using X-ray diffraction (XRD). Diffraction patterns of CeO_2, prCeO_2, and trCeO_2 (Fig. 1a) reveal characteristic peaks at 2θ ≈ 28.5°, 33°, 47.5°, 56.4°, and 69.4° corresponding to the (111), (200), (220), (311), and (222) planes of face-centered cubic fluorite ceria (JCPDS 034-0394). XRD indexing and the absence of non-ceria peaks confirm the successful synthesis of fluorite CeO_2 (see Fig. S1 for crystal and facet structures of CeO_2), the retention of the fluorite structure upon plasma and thermal reduction, and the absence of any XRD-detectable (i.e., crystalline) impurities. Compared to as-synthesized CeO_2, prCeO_2 and trCeO_2 exhibited narrower diffraction peaks with smaller Full Width at Half Maximum (FWHM) values (Table S1), indicating that plasma and thermal reduction induce growth in the average crystallite size. In nanostructured ceria, changes in crystallinity or lattice parameters are commonly associated with the formation of point defects, particularly V_o, and the concurrent formation of Ce^{3+} species with larger ionic radius, as well reported in the literature.[39, 52-54] We estimated the average crystallite size (D) and interplanar distance (d-spacing) for CeO_2, prCeO_2, and trCeO_2 using Scherrer's equation and Bragg's law (see Note S1 and Fig. S2 in the ESI).

The Scherrer analysis was performed without explicit correction for instrumental broadening, thereby resulting in apparent rather than absolute crystallite sizes. The calculated crystallite sizes (i.e., Scherrer widths) for CeO_2, $prCeO_2$, and $trCeO_2$ were 18.1, 21.7, and 20.9 nm, respectively (Table S2). The corresponding d-spacings (Table S3) for the (111), (200), and (220) facets showed no statistically significant differences among CeO_2, $prCeO_2$, and $trCeO_2$ within the resolution of laboratory XRD. For example, the (111) facet exhibited d-spacings of ~3.12, 3.12, and 3.13 Å for CeO_2, $prCeO_2$, and $trCeO_2$, respectively, indicating that plasma and thermal reduction do not result in an XRD-resolvable lattice expansion or contraction at the bulk-averaged level. Nevertheless, a qualitative comparison of peak positions (Fig. 1b) reveals a slight shift to higher 2θ values for $prCeO_2$, whereas $trCeO_2$ peaks exhibited a minor shift to lower 2θ values. The observed shifts are consistent with differences in strain distribution and defect localization rather than bulk lattice distortion, given the absence of statistically significant changes in bulk-averaged d-spacings. The rightward shift in the 2θ diffraction angles observed for $prCeO_2$ suggests subtle lattice contraction, consistent with surface densification and relaxation, where clustering of surface-localized V_o/Ce^{3+} pairs outweighs uniform bulk expansion[55, 56], likely a consequence of the highly energetic, surface-modifying, and non-equilibrium nature of the plasma environment. In contrast, the leftward shift in $trCeO_2$ is consistent with a more homogeneous distribution of V_o defects, where chemical expansion associated with Ce^{3+} formation throughout the bulk prevails under thermal treatment.[57, 58] Collectively, the observed FWHM narrowing, crystallite size growth, and subtle peak-shift trends support that both plasma and thermal reduction promote recrystallization and defect formation, where plasma reduction likely generates surface-concentrated defects while thermal reduction leads to a uniform distribution of defects. Nonetheless, the extent of defect formation and distribution are more reliably resolved by complementary spectroscopy techniques.[59]

To provide spectroscopic evidence of V_o defects in $prCeO_2$ and $trCeO_2$, we employed room-temperature Raman spectroscopy (Figs. 1c-e). The characteristic F_{2g} band located at ~466 cm^{-1} (Fig. 1c) is associated with symmetrical stretching of vibration of Ce-O_8 polyhedra, where each Ce^{4+} ion in the bulk is 8-fold coordinated with oxygen atoms[60] (see Fig. S3 for the crystal structure of fluorite CeO_2). The F_{2g} band for both $prCeO_2$ and $trCeO_2$ exhibited peak broadening and a red-shift to lower Raman shift values compared to as-synthesized CeO_2, indicative of increased lattice disorder and a higher concentration of Ce^{3+}.[61] Furthermore, the defect-sensitive D band at ~595 cm^{-1} (Fig. 1d), which intensifies with increasing V_o density due to lattice distortions[53, 62], is more prominent in $prCeO_2$ and $trCeO_2$ compared to as-synthesized CeO_2. The intensity ratio of the D to the F_{2g} bands (I_D/F_{2g})[60, 63] follows the trend $trCeO_2$ > $prCeO_2$ > CeO_2, suggesting that $trCeO_2$ exhibits the highest concentration of intrinsic defects. In this work, the I_D/F_{2g} ratio is employed as a relative descriptor of V_o density under identical Raman acquisition conditions, rather than as an absolute quantification of V_o concentration. Furthermore, we analyzed second-order bands, which are more sensitive to lattice disorders due to enhanced phonon-phonon interactions. The intensities of the second-order longitudinal optical (2LO) band at ~1180 cm^{-1} (Fig. 1e) and the second-order transverse optical (2TO) band at ~272 cm^{-1} (Fig. S4) increased in the order $trCeO_2$ > $prCeO_2$ > CeO_2, thereby reinforcing the findings from first-order F_{2g} and D bands. Collectively, the observed broadening and red-shift of the F_{2g} peaks, enhanced D band intensities, increased I_D/F_{2g} ratios, and the stronger second-order modes are all consistent with a higher concentration of V_o in $trCeO_2$ and $prCeO_2$ compared to untreated CeO_2.

In order to substantiate the generation of V_o from the perspective of paramagnetic Ce^{3+}, we analyzed CeO_2, $prCeO_2$, and $trCeO_2$ using electron paramagnetic resonance (EPR) spectroscopy. Compared to as-synthesized CeO_2, both $prCeO_2$ and $trCeO_2$ exhibited stronger EPR signals and a slight red-shift toward lower magnetic field values (Fig. S5), indicating an enhanced localization of unpaired 4f electrons and increased concentration of paramagnetic Ce^{3+} species. Upon Gaussian fitting of the EPR spectra (Fig. 1f), g-factor values of 1.9620, 1.9624, and 1.9627 were determined for CeO_2, $prCeO_2$, and $trCeO_2$, respectively (see Note S2 for g-factor calculations). While the g-factor variations are subtle, they are consistent with an increased density of V_o in $prCeO_2$ and $trCeO_2$, reflecting local electronic perturbations around Ce^{3+} sites due to plasma and thermal reductio.[64, 65] Analysis of the EPR signal linewidths (FWHM) from the integrated spectra (Fig. S6) reveals a progressive decrease (CeO_2 > $prCeO_2$ > $trCeO_2$), consistent with enhanced spin-exchange among Ce^{3+} species in reduced samples. We further analyzed the cavity Q-factor and EPR peak-to-peak linewidth trends (Table S4). The obtained Q-factor values were 4316, 3993, and 3614 for CeO_2, $prCeO_2$, and $trCeO_2$, respectively, indicating greater microwave losses in reduced samples. Similarly, the EPR spectra exhibited peak-to-peak linewidth values of 10.5, 9.5, and 8.6 G for CeO_2, $prCeO_2$, and $trCeO_2$, respectively, reinforcing the trend of enhanced spin-exchange interactions and higher defect concentrations in reduced samples. Overall, the EPR results and semi-quantitative descriptors corroborate the findings from Raman spectroscopy, confirming a higher concentration of V_o defect sites in $prCeO_2$ and $trCeO_2$ relative to untreated CeO_2.

Next, we utilized scanning electron microscopy (SEM) to understand the morphology and external structural features of the as-synthesized CeO_2, CeO_2@Zn-ZIF8, and CeO_2@Co/Zn-ZIF precursors. The SEM image of CeO_2 (Fig. 1g) reveals flower-like aggregates of thin flakes with a thickness of ~20 nm, whereas CeO_2-free Zn-ZIF8 particles exhibit a well-defined polyhedral morphology (Fig. S7) with an average particle size of ~200 nm. For CeO_2-embedded ZIF precursors, SEM images of both CeO_2@Zn-ZIF8 and CeO_2@Co/Zn-ZIF (Figs. 1h and 1i) indicate that the overall ZIF polyhedral morphology is largely preserved, while the encapsulation of CeO_2 particles is reflected in surface protrusions, roughened textures, and localized fragmentation or chipping.

To investigate the internal structure and elemental distribution of the CeO_2 and ZIF precursor components, we employed transmission electron microscopy (TEM) and scanning transmission electron microscopy coupled with electron energy loss spectroscopy (STEM-EELS). High-resolution TEM of CeO_2 (Fig. 1j) reveals clear fringes with a calculated d-spacing of 0.31 nm, corresponding to the (111) plane of cubic CeO_2. STEM-EELS elemental maps of CeO_2 (Fig. 1k) demonstrate a uniform distribution of Ce and O. The TEM image of an individual Zn-ZIF8 particle (Fig. 1l) further illustrates the polyhedral (rhombic dodecahedron) shape with a hexagonal cross-section and gradually fading contrast toward the particle edges, consistent

with reduced sample thickness at extremities. STEM-EELS elemental maps of Zn-ZIF8 particles (Fig. S8) display the uniform distribution of Zn, N, and C in the structure.

2.2 Thermal transformation and post-pyrolysis characterization

To elucidate the thermal transformation behavior of CeO_2 and ZIF precursor components during pyrolysis, we conducted thermogravimetric analysis (TGA) in the temperature range of 25-1000 °C under inert atmosphere. The TGA profiles of CeO_2, Zn-ZIF8, and Co/Zn-ZIF (Fig. 2a) highlight distinct mass-loss patterns. CeO_2 exhibited high thermal stability throughout the temperature range, with <10% mass loss, likely due to adsorbed moisture. In contrast, Zn-ZIF8 and Co/Zn-ZIF exhibited a major mass-loss event in the 550-650 °C region, corresponding to the decomposition of the 2-methylimidazole linkers via methyl-groups and imidazolate-ring breakdown.[66] Above 650 °C, the mass-loss in Co/Zn-ZIF was more pronounced compared to Zn-ZIF8, indicating that the presence of dual Co/Zn nodes negatively impacts the thermal stability of the framework. The superior thermal stability of CeO_2 highlights its suitability as a modifier to ZIF-derived electrocatalysts prepared via high-temperature pyrolysis.

Next, we compared the XRD patterns of the ceria@ZIF composite before and after pyrolysis to resolve structural evolution and probe phase transformations. For instance, diffraction patterns of pre-pyrolysis CeO_2@Co/Zn-ZIF and post-pyrolysis CeO_2@Co/N-C are shown in Fig. 2b, indexed against Zn-ZIF8 (simulated), Co (JCPDS 015-0806), and CeO_2 (JCPDS 034-0394) references. Diffraction patterns for CeO_2@Co/Zn-ZIF exhibited all the characteristic peaks of the CeO_2 and Zn-ZIF8 components, whereas CeO_2@Co/N-C retained only CeO_2 peaks. The disappearance of Zn-ZIF8 peaks and retention of CeO_2 indicate the carbonization of the ZIF framework while reinforcing the structural preservation of CeO_2 during pyrolysis. Furthermore, new peaks appeared for CeO_2@Co/N-C at $2\theta \approx$ 44.2°, 51.5°, and 75.9° corresponding to the (111), (200), and (220) facets of metallic Co. The appearance of metallic Co peaks is consistent with the formation of metallic nanoparticles (NPs) during the pyrolysis of Co-containing ZIF precursors[67-69], driven by the aggregation of Co nodes at high temperatures.

Complementary to the bulk crystallographic information from XRD, we employed STEM-EELS to investigate the impact of pyrolysis on the local morphology and elemental distribution in the final CeO_2@Co/N-C catalyst. Elemental maps (Fig. 2c) indicate that the ZIF shell maintained its skeletal shape with Co and CeO_2 nanoparticles embedded in the structure. Uniform distribution of N and C in the structure is observed, highlighting the transformation of the ZIF shell into an N-doped carbon matrix after pyrolysis.

2.3 Electrochemical properties and ORR performance

To evaluate the electrochemically accessible surface area (ECSA) of the developed electrocatalysts, we employed the electrochemical double-layer capacitance (C_{dl}) method. In the C_{dl} method, cyclic voltammograms (CVs) were collected in the non-Faradaic region of 0.9-1.0 V vs. RHE in Ar-saturated KOH (Fig. S9). The difference between cathodic and anodic current densities was plotted as a function of scan rate (Fig. 3a), and the C_{dl} value was extracted from the slope. Subsequently, the ECSA was determined from the C_{dl} using the specific capacitance and normalized by the mass of the deposited catalyst (see Note S3 in the ESI). The obtained C_{dl} and ECSA values (Table S5) reveal distinct structural and compositional effects. As-synthesized ceria (CeO_2) exhibited the lowest C_{dl} (0.13 mF/cm^2) and ECSA (3.25 m^2/g), reflecting the intrinsically poor electronic conductivity of ceria, which limits charge propagation and suppresses double-layer capacitance at the oxide-electrolyte interface. In contrast, ceria-free N-doped carbon (N-C) derived from Zn-ZIF8 exhibited markedly higher C_{dl} (8.5 mF/cm^2) and ECSA (212.5 m^2/g), consistent with a large accessible surface area and efficient charge transport. Among the Co-free ceria@N-C samples (i.e., CeO_2@N-C, prCeO_2@N-C, and trCeO_2@N-C), prCeO_2@N-C exhibited the highest C_{dl} (12.4 mF/cm^2) and ECSA (310 m^2/g), with the trend prCeO_2@N-C > trCeO_2@N-C > CeO_2@N-C indicating that V_o enhance interfacial charge accumulation and ion accessibility. A similar trend was observed for the ceria@Co/N-C sample series, where CeO_2@Co/N-C exhibited lower C_{dl} and ECSA values compared to V_o-rich prCeO_2@Co/N-C and trCeO_2@Co/N-C. Relative to ceria-free N-C and Co/N-C, incorporation of as-synthesized CeO_2 reduces the C_{dl} and ECSA, whereas V_o-rich ceria partially restores or enhances these values, highlighting the beneficial role of defective ceria in promoting electrochemically accessible interfaces. Furthermore, the presence of Co NPs reduces the overall capacitance compared to Co-free ceria@N-C samples, likely due to partial coverage of the conductive carbon network. Collectively, these results demonstrate that V_o-rich ceria can enhance the electrochemically accessible surface area. Meanwhile, metallic Co NPs increase the overall catalyst mass without proportionally contributing to double-layer capacitance, which lowers the accessible surface area per unit mass and limits electrolyte-accessible N-doped carbon sites. It is important to note that the C_{dl} method utilized herein accounts for capacitance contributions from the entire carbon-electrolyte interface, including both catalytic and non-catalytic surfaces, and thus may overestimate the intrinsic electrochemically active surface area. Thus, the ECSA values reported herein should be interpreted primarily as relative comparative metrics across each catalyst series rather than absolute measures of true active-site density.

We further probed the interfacial charge-transfer characteristics using electrochemical impedance spectroscopy (EIS). Measurements were conducted in O_2-saturated 0.1 M KOH under quiescent conditions (no rotation). The resulting Nyquist plots (Fig. 3b) were fitted (Fig. S10 and Table S6) with an equivalent circuit model accounting for solution resistance (R_s), interfacial charge-transfer resistance (R_{ct}), a constant phase element (CPE), and Warburg diffusion elements (see Note S4 for more details). As-synthesized CeO_2 exhibited a significantly higher R_{ct} (48.0 Ω) than all ZIF-derived materials (26.7-30.9 Ω), reflecting sluggish charge-transfer due to its intrinsically low conductivity. In contrast, R_{ct} was comparable across all ceria@N-C and ceria@Co/N-C electrocatalysts, indicating similar electron transfer kinetics once conductive carbon frameworks are present. While differences in the low-frequency impedance response were observed across samples, the analysis and interpretation of diffusion-related parameters are highly model-dependent. Therefore, a detailed yet cautious discussion of the low-frequency impedance and fitting parameters, alongside the Bode plot analysis (Figs. S11a and S11b), is provided in the ESI.

Collectively, the EIS results demonstrate that the conductive

carbon matrix effectively mitigates the charge-transfer limitations of ceria and that while oxygen vacancies can enhance ion diffusion of ceria@N-C hybrid structures, their influence becomes secondary to the dominant effects introduced by metallic Co NPs in ceria@Co/N-C samples.

Next, CVs were collected in Ar- and O_2-saturated 0.1 M KOH (Fig. 3c) to investigate the redox behavior of ceria@N-C and ceria@Co/N-C electrocatalysts. Under O_2 saturation, all electrocatalysts showed a reduction peak around 0.7 V vs. RHE, whereas no peaks appeared under Ar saturation, indicating that the observed cathodic peaks arise from oxygen reduction. Co-free ceria@N-C electrocatalysts (i.e., CeO_2@N-C, prCeO_2@N-C, and trCeO_2@N-C) exhibited more capacitive CV profiles with enhanced capacitive currents, consistent with their higher ECSAs. Notably, the reduction peaks of electrocatalysts embedding defective prCeO_2 and trCeO_2 were slightly shifted to more positive potentials compared to electrocatalysts embedding as-synthesized CeO_2, suggesting that V_o might contribute to more favorable ORR kinetics. The magnitude of capacitive currents and right-shift in the position of the reduction peak followed the order of prCeO_2@N-C > trCeO_2@N-C > CeO_2@N-C for ceria@N-C samples and prCeO_2@Co/N-C > trCeO_2@Co/N-C > CeO_2@Co/N-C for ceria@Co/N-C samples, consistent with their ECSA trends. Overall, the CV profiles confirm the ORR activity of all ceria@N-C and ceria@Co/N-C electrocatalysts, with V_o-rich ceria variants exhibiting more positive shifts in the reduction peak.

Next, we evaluated the ORR performance of the developed electrocatalysts in 0.1 M KOH using the RRDE setup (Fig. S12). Prior to testing, the collection efficiency of the ring electrode was calibrated and the collection efficiency was determined (refer to Note S5 and Fig. S13 in the ESI). Figures 4a–c display the ORR polarization curves collected at a rotation speed of 1600 rpm. Among ceria@N-C samples (Fig. 4a), V_o-rich prCeO_2@N-C and trCeO_2@N-C exhibited more positive onset (E_{onset}) and half-wave ($E_{1/2}$) potentials than CeO_2@N-C, indicating improved ORR performance. Nonetheless, all ceria@N-C samples exhibited lower E_{onset}, $E_{1/2}$, and ring currents compared to ceria-free N-C, yet achieved higher mass transport limited current densities, suggesting either improvements in mass transport and/or selectivity towards the 4e$^-$ reduction mechanism. For ceria@Co/N-C samples (Fig. 4b), V_o-rich prCeO_2@Co/N-C and trCeO_2@Co/N-C had increased ring currents and E_{onset} and $E_{1/2}$ values that were slightly more positive than CeO_2@Co/N-C. Nonetheless, ceria-free Co/N-C outperformed all ceia@Co/N-C samples in E_{onset}, $E_{1/2,}$ and diffusion-limited currents, suggesting that ceria and its deficiency alter the ORR selectivity, whereas Co-based sites and the content of Co are likely the dominant performance drivers in these samples. A direct comparison between trCeO_2@N-C and trCeO_2@Co/N-C (Fig. 4c), as the samples embedding the most defective ceria, highlights the vastly different ORR activity between Co-free and Co-containing samples, indicating that ceria plays a secondary yet modulatory in tuning ORR performance. Within each host series, prCeO_2@N-C and prCeO_2@Co/N-C, embedding more surface-biased defect structures, exhibited more favorable ORR metrics than their trCeO_2-based analogues, highlighting that accessibility distribution of V_o centers are more influential than total defect density. Thus, the true effect of ceria and its defects is likely electronic interaction with the carbon matrix or Co nanoparticles through interfacial interactions. The corresponding H_2O_2 selectivity (Figs. 4d-f) reveal the trends trCeO_2@N-C > prCeO_2@N-C > CeO_2@N-C for ceria@N-C samples and trCeO_2@Co/N-C > prCeO_2@Co/N-C > CeO_2@Co/N-C for ceria@Co/N-C samples, confirming a positive correlation between oxygen defects and 2e$^-$ ORR/HO_2^- selectivity. For trCeO_2@N-C and trCeO_2@Co/N-C, as the samples with the highest V_o-concentration, the maximum selectivity towards HO_2^- reached ~27% and 18%, respectively. All ceria@Co/N-C samples exhibited lower HO_2^- selectivity than ceria@N-C samples, due to the presence of Co NPs interfacing with N-doped carbon, which favor 4e$^-$ ORR.[70, 71] Comparing against ceria-free N-C and Co/N-C references, however, reveals distinct mechanistic insights that suggest microenvironment-dependent impact of V_o. In Co-free systems, despite trCeO_2@N-C exhibiting the highest HO_2^- selectivity amongst ceria@N-C samples, the selectivity remains significantly lower (18-70% depending on the potential) than ceria-free N-C, potentially due to Ce^{3+}-V_o centers promoting mixed 2e$^-$/4e$^-$ pathways via partial O-O bond breakage at the ceria-carbon interface[42], partially offsetting the inherently 2e$^-$ ORR-selective N-C. In Co-containing samples, trCeO_2@Co/N-C exhibited higher HO_2^- selectivity than ceria-free Co/N-C, suggesting that V_o suppresses the Co NP-driven 4e$^-$ ORR, potentially due to Co-CeO_2 interactions causing charge redistribution typical in transition metal-ceria interfaces.[44, 72] Although Co nanoparticles remain the primary contributors to 4e$^-$ ORR activity, systematic differences in HO_2^- selectivity within each ceria@Co/N-C series indicate that defective ceria actively modulates pathway selectivity through interfacial electronic interactions. Specifically, V_o-rich ceria partially suppresses Co-driven 4e$^-$ ORR behavior, consistent with Ce^{3+}/V_o-rich interfaces altering oxygen adsorption energetics and stabilizing intermediates associated with the 2e$^-$ pathway.[54, 72] The average electron transfer number (Fig. 4g) corroborates CeO_2@N-C and CeO_2@Co/N-C, which embed as-synthesized CeO_2, having the highest electron transfer numbers (i.e., lowest H_2O_2 selectivity) of 3.4 and 3.8 amongst ceria@N-C and ceria@Co/N-C electrocatalysts, respectively. All ceria@N-C samples exhibited electron transfer numbers <3.5, whereas all ceria@Co/N-C samples exhibited electron transfer numbers >3.5, regardless of ceria-embedding or V_o-richness. Overall, catalysts containing V_o-rich ceria showed improved kinetics compared to catalysts containing as-synthesized ceria. Nonetheless, defective ceria modulated ORR mechanisms differently by weakening 2e$^-$ ORR in N-C by introducing mixed pathways, while partially suppressing Co NP-driven 4e$^-$ ORR in Co/N-C via interfacial electronic coupling, hence making the impact of V_o on ORR pathway host- and microenvironment-dependent. These observations further suggest that ORR performance is governed by an optimal defect configuration, where surface and electrochemically accessible V_o centers are more beneficial than a simple monotonic increase in bulk defect density. While direct spectroscopic confirmation of electronic state changes of Ce, N, and Co at the ceria-host interface remains an important direction for future work, the convergence of structural defect signatures with systematic electrocatalytic trends supports the interpretation that V_o-rich ceria acts as an electronic modifier of the ZIF-derived host matrices.[73, 74]

To decouple intrinsic catalytic activity from electrochemical surface area effects, we calculated the ECSA-normalized activity

(j_{ECSA}), obtained by normalizing the kinetic current density (j_k) with the corresponding ECSA values (see Note S6 and Table S7 in the ESI). The resulting j_{ECSA} values follow the order N-C > $trCeO_2$@N-C > $prCeO_2$@N-C > CeO_2@N-C and Co/N-C > $trCeO_2$@Co/N-C > $prCeO_2$@Co/N-C > CeO_2@Co/N-C for each sample series, respectively. For the Co-free series (Fig 4h), it is evident that N-C exhibits a higher j_{ECSA} (0.15 μA/cm^2) than CeO_2@N-C (0.04 μA/cm^2) and $trCeO_2$@N-C (0.06 μA/cm^2) which contain as-synthesized and V_o-rich ceria, respectively. This trend suggests that while V_o-richness in ceria positively impacts reactivity, the introduction of ceria partially dilutes or passivates the density of ORR active-sites, leading to a trade-off between electronic modulation and activity. A similar trend is observed for the Co-containing series (Fig. 4i), where ceria-free Co/N-C exhibits a higher j_{ECSA} (3.67 μA/cm^2) relative to CeO_2@Co/N-C and $trCeO_2$@Co/N-C (0.9-1.2 μA/cm^2), consistent with ceria suppressing the 4e$^-$ ORR activity of Co NPs. Collectively, despite enhancing the ECSA, ECSA-normalized activity reveals that the primary influence of oxygen-defects is in tuning ORR selectivity, but can compromise intrinsic ORR activity when embedded within ZIF-derived electrocatalysts. Since all ceria-modified catalysts were prepared with a fixed ceria loading, the observed differences in ECSA, selectivity, and ORR activity are attributed to ceria defect chemistry rather than variations in oxide fraction. Nonetheless, systematic variation of the CeO_2:N-C or CeO_2:Co/N-C ratio may further tune the balance between conductivity, accessibility, and electronic modulation and can be systematically explored in future work.

To evaluate the impact of embedding defective ceria on the stability of the ZIF-derived electrocatalysts, 8-hour chronoamperometry tests were conducted at 0.1 V vs. RHE in the RRDE configuration (Fig. 4j). The comparison between $trCeO_2$@N-C and N-C (left panel) shows comparable disk current retentions, both showing a slight increase of ~0.5-3% after 8 hours, indicating no adverse effects of ceria embedding on the degradation of the ZIF-derived N-C and Co/N-C structures or electrochemical stability. However, ring currents for $trCeO_2$@N-C remained more stable over time compared to N-C, which showed measurable fluctuations and a gradual decay, suggesting that the Ce^{3+}/C^{4+} redox couple and V_o in $trCeO_2$ stabilize the local ORR reaction environment and the production of HO_2^-. In contrast, both $trCeO_2$@Co/N-C and Co/N-C (right panel) retained >96.5% of their initial disk current, yet exhibited slightly increasing ring currents over time, implying a destabilizing role of Co NPs, likely due to surface restructuring/passivation and altered surface reaction equilibria diminishing its ORR activity, thus outweighing the stabilizing role of ceria. Overall, the results from the two sample series indicate that the main determinant of performance stability in these hybrid systems is the presence of Co NPs rather than ceria. The role of Ce^{3+}/V_o and their effect on the ORR pathway becomes more evident under higher mass-transport and local oxygen flux conditions, such as in the gas-diffusion electrode.

To quantitatively evaluate peroxide generation and further elucidate the influence of oxygen vacancies on the 2e$^-$ ORR pathway, we performed chronoamperometric measurements on a carbon gas-diffusion electrode in a low-volume H-Cell (Fig. S14). The potential was held at 0.1 V vs. RHE for 30 minutes, after which 1 mL sample from the catholyte was withdrawn and analyzed by UV-VIS (see section 4.5 for details). The chronoamperometric responses of bare carbon paper (CP), N-C, and $trCeO_2$@N-C (Fig. 5a) reveal distinct current-time profiles. The bare CP, serving as a control, exhibited low currents (<4.5 mA), confirming its negligible intrinsic ORR activity. N-C displayed a higher steady-state current, consistent with its abundant N-doped carbon active sites and high intrinsic 2e$^-$ ORR activity. In contrast, $trCeO_2$@N-C showed ~20% higher overall current densities yet led to lower H_2O_2 yield rate (Fig. 5b and Table S8).

The quantified H_2O_2 yield rate followed the order N-C > $trCeO_2$@N-C > CP, indicating that embedding V_o-rich ceria suppresses peroxide formation and/or accumulation despite improved ORR currents. Overall, these H-cell results suggest that defective $trCeO_2$ promotes partial O-O bond cleavage and facilitate mixed 2e$^-$/4e$^-$ pathways through Ce^{3+}/V_o sites and electronic modulating at the ceria-carbon, thereby consuming in-situ-generated H_2O_2 intermediates or further reducing them to H_2O, consistent with the RRDE observations.

The findings and observed trends in this work are better understood when contextualized with prior ceria-modified ORR electrocatalyst studies. Previous reports have demonstrated enhanced activity and stability of N-C and M-N_x/C catalysts upon ceria incorporation, often attributed to radical scavenging or charge transfer of Ce 4f electrons to N-doped carbon and transition metal catalysts.[75-78] However, our ceria defect-engineering in a multi-host approach reveals a more nuanced function for V_o. While V_o-rich ceria acts as a structural and electronic modulator, its influence on 2e$^-$/4e$^-$ ORR selectivity is strongly host-dependent and governed by the nature of the surrounding active sites. For instance, in Co-free N-C hosts, whose N-doped sites are intrinsically selective for the 2e$^-$ pathway, Ce^{3+}/V_o centers promoted mixed 2e$^-$/4e$^-$ pathways, partially reducing HO_2^- and increasing current. In contrast, in Co/N-C hosts, in a Co/N-C host, where Co NP drive selective 4e$^-$ pathway, V_o modulates the Co-driven 4e$^-$ pathway, lowering HO_2^- production without substantially enhancing activity. It is also noteworthy to highlight that previous works rely mostly on in-situ growth of ceria to achieve optimized heterostructures and controlled morphologies (e.g., nanospheres, nanorods, and nanocubes). Nonetheless, ceria nanostructures in this work are pre-synthesized and treated before integration into ceria@N-C and ceria@Co/N-C electrocatalysts, which enables independent control over ceria defect chemistry but hinders optimal ceria loadings and ceria-support heterojunctions for peak ORR activity.

3 Conclusions

In this study, we systematically elucidated how defective ceria can modulate the selectivity of ORR electrocatalysts derived from Zn-ZIF8 and Co/Zn-ZIF precursors. Plasma and thermal reduction were employed to prepare V_o-rich $prCeO_2$ and $trCeO_2$, respectively. Ceria variants were subsequently embedded within Zn-ZIF8 and Co/Zn-ZIF, via a one-pot synthesis method, and pyrolyzed at 900 °C to prepare ceria@N-C and ceria@Co/N-C electrocatalysts. Structural and spectroscopic characterization confirmed the successful introduction of V_o, with $prCeO_2$ exhibiting surface-concentrated vacancies and $trCeO_2$ exhibiting the highest concentration of bulk distributed V_o. Thermal transformation analysis of the ceria and ZIF precursors revealed that ceria retains its structural integrity during pyrolysis, while ZIF frameworks are transformed into N-doped carbons. Post-pyrolysis

characterization of the electrocatalysts revealed morphology collapse and uniform distribution of N and C in the N-doped carbon structure, while polydisperse metallic Co NPs nucleate in samples derived from Co/Zn-ZIF.

Electrochemical properties and ORR performance, evaluated in 0.1 M KOH, revealed that in Co-free systems, V_o-rich ceria acted primarily as an electronic modulator at the ceria-carbon interface. While it enhanced charge transfer and electrochemically accessible surface area, it also introduced mixed $2e^-/4e^-$ ORR pathways, thereby partially offsetting the inherent $2e^-$ selectivity of the N-C matrix. In contrast, in the Co-containing ceria@Co/N-C series, the presence of metallic Co NPs dictated the primary activity. Here, V_o-rich ceria played a different role: it engaged in electronic metal-support interactions with the Co NPs, causing interfacial charge redistribution that subtly suppressed the Co NP-driven $4e^-$ pathway. ECSA-normalized activity revealed that V_o-rich ceria partially dilutes the intrinsic density of active sites, establishing a trade-off between electronic tuning and site availability. Chronoamperometric stability tests demonstrated that Ce^{3+}/V_o centers stabilize reactive intermediates and mitigate peroxide-induced degradation, whereas Co NPs caused mild current drift likely associated with surface restructuring under alkaline conditions.

Overall, this work highlights the impact of V_o-rich ceria in structurally and electronically modifying ZIF-derived N-C and Co/N-C ORR electrocatalysts, demonstrating that V_o in ceria are not mere activity or stability promoters but are versatile knobs that can be tuned to steer ORR pathway selectivity based on the host architecture. These insights advance defect-engineering strategies toward rational design of durable, selective, and application-specific PGM-free electrocatalysts to tackle performance bottlenecks and advance ORR-based technologies. For future investigations, the relationship between Co nanoparticle size and ORR performance in ceria-modified Co/N-C electrocatalysts, and its synergy with defective ceria, warrants a systematic investigation. Furthermore, direct spectroscopic confirmation of electronic state changes of Ce, N, and Co at the ceria-host interface, via element-specific spectroscopic techniques like X-ray absorption spectroscopy (XAS), represents an important direction for future studies.

4 Experimental

4.1 Chemicals

Cerium(III) acetate hydrate (99.9% trace metal basis), zinc nitrate hexahydrate (reagent grade, 98%), cobalt nitrate hexahydrate (ACS reagent, ≥ 98%), 2-methylimidazole (99%), potassium hydroxide (ACS reagent, ≥ 85% pellets), potassium ferricyanide(III), and cerium(IV) sulfate tetrahydrate were purchased from Sigma-Aldrich. Nafion (5 wt.%, Ion Power), Teflon-treated Sigracet 39BB carbon paper, and Fumasep FAB-PK-130 anion exchange membrane were purchased from Fuel Cell Store. Ultrapure type 1 Milli-Q water (resistivity ≥ 18.2 MΩ · cm) was used for electrolyte preparation. All chemicals were used as received without further purification.

4.2 Preparation of precursors and electrocatalysts

4.2.1 Synthesis of CeO_2, $prCeO_2$, and $trCeO_2$

CeO_2 was synthesized according to a previously reported procedure.[79] In a combustion boat, 400 mg of cerium(III) acetate was loaded and subjected to a two-stage annealing process using a tube furnace (Lindberg/Blue M). The temperature was ramped up at a rate of 5 °C/min, held at 350 °C for 2 hours, and then at 600 °C for 5 hours. $trCeO_2$ was prepared via annealing the CeO_2 powder in a reductive environment (3% H_2/N_2). In a combustion boat, 200 mg of CeO_2 was loaded and annealed at 400 °C for 3 hours under the reductive gas flow. The temperature was ramped up at 5 °C/min. $prCeO_2$ was prepared via treating the CeO_2 powder with air plasma in a benchtop plasma treatment instrument (Harrick Plasma). 200 mg of CeO_2 was loaded into a 20 mL glass vial and treated with air plasma for 6 minutes at a radio frequency power of 45 W.

4.2.2 Synthesis of ceria@ZIF precursors

All ceria@ZIF precursors were synthesized with a nominal ceria loading of ~10 wt.% relative to the ZIF framework to balance ceria-induced modulation with preservation of the host's conductivity and accessibility sites. First, 180 mg of ceria powder (CeO_2, $prCeO_2$, or $trCeO_2$) was suspended in 70 mL of methanol. The solution was sonicated for 15 minutes to disperse the particles and fragment the ceria flakes. Then, 3.2 g of 2-methylimidazole were added to the solution, while being vigorously stirred, followed by 1.5 g of $Zn(NO_3)_2 \cdot 6H_2O$ to grow Zn-ZIF8 shells. The solution was left vigorously stirring for 10 hours. The product was then recovered via two centrifugation steps at 10,000 rpm with methanol solvent exchange to remove residual reactants, followed by an ethanol/water wash to ensure purity. Finally, the product was dried in an oven at 75 °C overnight. The same procedure was followed, but with the addition of a 1:1 weight ratio of $Zn(NO_3)_2 \cdot 6H_2O$ and $Co(NO_3)_2 \cdot 6H_2O$ to grow the bimetallic Co/Zn-ZIF shell. Samples embedding as-synthesized ceria are labeled CeO_2@Zn-ZIF8, and CeO_2@Co/Zn-ZIF. Samples embedding plasma-reduced ceria are labeled $prCeO_2$@Zn-ZIF8 and $prCeO_2$@Co/Zn-ZIF. Samples embedding thermally-reduced ceria are labeled $trCeO_2$@Zn-ZIF8, and $trCeO_2$@Co/Zn-ZIF. Complementary gas-diffusion electrode experiments confirmed that defective ceria suppresses peroxide accumulation by facilitating in situ consumption or further reduction of H_2O_2 intermediates, consistent with mixed $2e^-/4e^-$ pathways.

4.2.3 Preparation of electrocatalysts

To prepare the final electrocatalysts, 400 mg of each ceria@ZIF precursor (i.e., CeO_2@Zn-ZIF8, CeO_2@Co/Zn-ZIF, $prCeO_2$@Zn-ZIF8, $prCeO_2$@Co/Zn-ZIF, $trCeO_2$@Zn-ZIF8, and $trCeO_2$@Co/Zn-ZIF) powder was placed in a 7 mL porcelain combustion boat and annealed in a tube furnace (Lindberg/Blue M, Thermo Scientific) at 900 °C for 2 hours under Ar flow. Pyrolysis was performed at 900 °C based on previous investigations into the thermal transformation of Co/Zn-ZIF-derived catalysts[67-69, 80] providing a balance between framework graphitization, electric conductivity, preservation of morphology, and retention of nitrogen content in the ZIF-derived carbon matrix. Samples embedding as-synthesized ceria are labeled CeO_2@N-C and CeO_2@Co/N-C. Samples embedding plasma-reduced ceria are labeled $prCeO_2$@N-C and $prCeO_2$@Co/N-C. Samples embedding thermally-reduced ceria are labeled $trCeO_2$@N-C and $trCeO_2$@Co/N-C.

4.3 Material characterization

Powder X-ray diffraction (XRD) was conducted with a Cu Kα

source in the 2θ range 5-95° to investigate the crystallinity of CeO_2 and CeO_2@ZIF precursors as well as the post-pyrolysis electrocatalysts. To probe the oxygen vacancy generation, Raman spectra were collected using a Renishaw InVia Raman spectrometer equipped with a 532 nm laser operated at 5 and 100 mW using a 1800 L/mm grating. For each sample, the reported spectra represent averages of measurements collected at three distinct positions under identical acquisition conditions. Measurements were also collected at different laser powers to confirm the reproducibility of observed spectral trends. Electron paramagnetic resonance (EPR) measurements were conducted in a continuous wave spectrometer (Bruker, EMXnano) operating at X-band (9.45 GHz), 100 kHz magnetic field modulation frequency, and 5 G modulation amplitude. The microwave power level was varied (2.5-25 mW). The thermal stability of CeO_2, $prCeO_2$, and $trCeO_2$ was evaluated through thermogravimetric analysis (TGA) using a thermal analyzer (TGA/DSC3+, Mettler Toledo) in the temperature range of room temperature to 1000 °C (10 °C/min) under Ar atmosphere. Scanning electron microscopy (SEM) was performed on a field emission scanning electron microscope (JSM-7000F, JEOL) at 30 kV. Transmission electron microscopy (TEM) was carried out on an aberration-corrected electron microscope (Talos 200x, Thermo Scientific) at 200 kV. Chemical information and elemental maps were obtained via electron-energy loss spectroscopy (EELS) in the scanning transmission electron microscopy (STEM) mode. UV-Vis measurements were conducted using a UV-Vis spectrophotometer (Tecan, Spark 10M) at a wavelength of 316 nm with a calibration range of 280-420 nm.

4.4 Preparation of inks and electrodes

To prepare inks for electrocatalysts for subsequent deposition as thin-films, 10 mg of each electrocatalyst was suspended in 600 µL of Iso-propanol and 1800 µL of ultrapure type 1 Milli-Q water (3:1 water to alcohol ratio). The ink was then sonicated for 30 minutes in an ice bath. Once the ink was homogeneous, 80 µL of Nafion (5 wt.%) was added, and the ink was vortexed for 5 minutes before drop-casting. To deposit each electrocatalyst as a thin-film for electrochemical testing, a 10 µL aliquot of the ink was drop-casted on the glassy carbon working electrode. All electrode loadings in this study were 0.2 $mg_{cat.}/cm^2$. For H_2O_2 quantification experiments, electrocatalysts were drop-casted on a 0.5 cm^2 teflon-treated carbon paper (Sigracet 39BB) with 0.4 $mg_{cat.}/cm^2$ catalyst loading.

4.5 Electrochemical measurements

Cyclic voltammetry and rotating ring-disk electrode (RRDE) hydrodynamic experiments were conducted in a 3-electrode cell using an Ag/AgCl (saturated KCl) reference electrode, a conductive graphite rod counter electrode, and an RRDE tip with a glassy carbon disk (5 mm diameter) and Pt ring (6.5 mm and 7.5 mm inner and outer diameters, respectively) working electrodes. A Biologic VSP 300 multichannel potentiostat was used for voltammetric and chronoamperometric measurements, and the WaveVortex 10 (Pine Research) rotator for rpm control in RRDE experiments. Experiments in alkaline media were conducted in 0.1 M KOH (pH=13). Before any ORR experiments, the electrolytes were purged with Ar for 20 minutes to determine and later subtract background currents. The electrolyte was purged with O_2 for voltammetric and chronoamperometric ORR measurements. All potentials were converted to the reversible hydrogen electrode (RHE) scale. Potentials were *iR*-corrected using the measured solution resistance (R_s) obtained from high-frequency EIS. Polarization curves were collected at different rotation speeds (100-2500 rpm) while holding the potential of the Pt ring (1.2 V vs. RHE) and sweeping the potential at the GC disk (0.05 to 1 V vs. RHE) with a scan rate of 20 mV/s. The collection efficiency (N) was calibrated in 1 M KCl with 0.1 mM potassium ferricyanide ($K_3[Fe(CN)_6]$) (Fig. S13). The electron transfer number (n) and HO_2^- selectivity were calculated according to the equations below:

$$n = \frac{I_{Disk}}{I_{Disk} + \frac{I_{Ring}}{N}} \quad (1)$$

$$HO_2^- \ selectivity\ (\%) = 200 \times \frac{\frac{I_{Ring}}{N}}{I_{Disk} + \frac{I_{Ring}}{N}} \quad (2)$$

EIS measurements were conducted at 0.45 V vs. RHE in the frequency range of 1 MHz to 100 mHz with a 750 mV sinus amplitude. To quantify H_2O_2, 30-minute chronoamperometric experiments were conducted in a two-compartment H-cell at 0.1 V vs. RHE. A Fumasep (FAB-PK-130) anion exchange membrane was used as a separator. The membrane was soaked in 1 M KOH overnight before use. Cathode and anode chambers were filled with 11 mL of 0.1 M KOH each. The HO_2^- generated at the cathode is converted to H_2O_2, upon mixing with an acidic cerium sulfate solution (0.5 M H_2SO_4) and the concentration of H_2O_2 was determined by colorimetric titration with cerium sulfate.

$$2Ce^{4+} + H_2O_2 \rightarrow 2Ce^{3+} + 2\,H^+ + O_2$$

The Ce^{4+} concentration-absorbance calibration curve (Fig. S15) was obtained by dilutions from the 1 mM $Ce(SO_4)_2$ in 0.5 M H_2SO_4 starting solution (0-0.8 mM). 1 mL of the electrolyte was withdrawn from the cathode chamber, mixed with the 1 mM $Ce(SO_4)_2$ solution, and the absorption at the wavelength of 316 nm was used to determine the concentration of Ce^{4+}/H_2O_2.

Acknowledgements

We would like to acknowledge the support of the department of chemical engineering at McMaster University and the generous funding of the National Research Council of Canada (NRC) under their Materials for Clean Fuels Challenge program. Electron microscopy experiments were done at the Canadian Centre for Electron Microscopy (CCEM). Powder X-ray diffraction was performed at the McMaster Analytical X-ray Diffraction Facility (MAX).

Conflicts of interest

There is no conflict of interest.

References

1. L. Carrette, K. A. Friedrich and U. Stimming, Fuel Cells: Principles, Types, Fuels, and Applications, *ChemPhysChem*, 2000, 1,

162-193.

2. A. B. Stambouli and E. Traversa, Fuel cells, an alternative to standard sources of energy, *Renewable and Sustainable Energy Reviews*, 2002, 6.

3. M. Winter and R. J. Brodd, What are batteries, fuel cells, and supercapacitors?, *Chemical Reviews*, 2004, 104, 4245− 4269.

4. Moving forward with fuel cells, *Nature Energy*, 2021, 6, 451.

5. M. A. Rahman, X. Wang and C. Wen, High energy density metal-air batteries: A review, *Journal of The Electrochemical Society*, 2013, 160, A1759-A1771.

6. L. Li, Z. w. Chang and X. B. Zhang, Recent progress on the development of metal-air batteries, *Advanced Sustainable Systems*, 2017, 1, 1700036.

7. F. Cheng and J. Chen, Metal–air batteries: from oxygen reduction electrochemistry to cathode catalysts, *Chemical Society Reviews*, 2012, 41, 2172.

8. S. Yang, A. Verdaguer-Casadevall, L. Arnarson, L. Silvioli, V. Čolić, R. Frydendal, J. Rossmeisl, I. Chorkendorff and I. E. Stephens, Toward the decentralized electrochemical production of H_2O_2: A focus on the catalysis, *ACS Catalysis*, 2018, 8, 4064-4081.

9. E. Jung, H. Shin, W. Hooch Antink, Y.-E. Sung and T. Hyeon, Recent Advances in Electrochemical Oxygen Reduction to H_2O_2: Catalyst and Cell Design, *ACS Energy Letters*, 2020, 5, 1881-1892.

10. S. Siahrostami, H_2O_2 electrosynthesis and emerging applications, challenges, and opportunities: A computational perspective, *Chem Catalysis*, 2023, 3, 100568.

11. C. Chen and T. Fuller, H_2O_2 Formation under Fuel-Cell Conditions, *ECS Transactions*, 2007, 11, 1127-1137.

12. K. Hongsirikarn, X. Mo, J. G. Goodwin and S. Creager, Effect of H_2O_2 on Nafion® properties and conductivity at fuel cell conditions, *Journal of Power Sources*, 2011, 196, 3060-3072.

13. E. Wallnöfer-Ogris, F. Poimer, R. Köll, M.-G. Macherhammer and A. Trattner, Main degradation mechanisms of polymer electrolyte membrane fuel cell stacks – Mechanisms, influencing factors, consequences, and mitigation strategies, *International Journal of Hydrogen Energy*, 2024, 50, 1159-1182.

14. P. C. Okonkwo, I. Ben Belgacem, W. Emori and P. C. Uzoma, Nafion degradation mechanisms in proton exchange membrane fuel cell (PEMFC) system: A review, *International Journal of Hydrogen Energy*, 2021, 46, 27956-27973.

15. Q. Liu, Z. Pan, E. Wang, L. An and G. Sun, Aqueous metal-air batteries: Fundamentals and applications, *Energy Storage Materials*, 2020, 27, 478-505.

16. F. Lai, H. Shang, Y. Jiao, X. Chen, T. Zhang and X. Liu, Recent progress and perspective on electrocatalysis in neutral media: Mechanisms, materials, and advanced characterizations, *Interdisciplinary Materials*, 2024, 3, 492-529.

17. T. G. Vo, J. Gao and Y. Liu, Recent Development and Future Frontiers of Oxygen Reduction Reaction in Neutral Media and Seawater, *Advanced Functional Materials*, 2024, 34.

18. Y. Jiang, Y. Jiang, H. Fu, H. Fu, Z. Liang, Z. Liang, Q. Zhang, Q. Zhang, Y. Du and Y. Du, Rare earth oxide based electrocatalysts: synthesis, properties and applications, *Chemical Society Reviews*, 2024, 53.

19. C. Li, P. Wang, M. He, X. Yuan, Z. Fang and Z. Li, Rare earth-based nanomaterials in electrocatalysis, *Coordination Chemistry Reviews*, 2023, 489.

20. X. Wang, Y. Tang, J.-M. Lee and G. Fu, Recent advances in rare-earth-based materials for electrocatalysis, *Chem Catalysis*, 2022, 2, 967-1008.

21. X. Man, Y. Chang and J. Jia, Rare-earth-based catalysts for oxygen reduction reaction, *Molecular Catalysis*, 2024, 565, 114389.

22. X. Wang, Y. Zhu, H. Li, J. M. Lee, Y. Tang and G. Fu, Rare-earth single-atom catalysts: a new frontier in photo/electrocatalysis, *Small Methods*, 2022, 6, 2200413.

23. R. Luo, R. Wang, Y. Cheng, Z. Meng, Y. Wang, Z. Guo, B. B. Xu, Y. Xia and H. Tang, Yttrium Oxide Nanoclusters Boosted Fe-N_4 and Fe_4N Electrocatalyst for Future Zinc–Air Battery, *Advanced Functional Materials*, 2024, 34.

24. S. K. Parida, B. A. Chalke, G. Kaur, A. K. Yadav and H. Jena, A Metal–Organic Framework-Derived Atomically Dispersed Yttrium as an Electrocatalyst for Oxygen Reduction Reaction, *ACS Applied Energy Materials*, 2024, https://doi.org/10.1021/acsaem.3c02911.

25. L. Yin, S. Zhang, M. Sun, S. Wang, B. Huang and Y. Du, Heteroatom-Driven Coordination Fields Altering Single Cerium Atom Sites for Efficient Oxygen Reduction Reaction, *Advanced Materials*, 2023, 35.

26. C. Fan, X. Wang, X. Wu, Y. Chen, Z. Wang, M. Li, D. Sun, Y. Tang and G. Fu, Neodymium-Evoked Valence Electronic Modulation to Balance Reversible Oxygen Electrocatalysis, *Advanced Energy Materials*, 2023, 13, 2203244.

27. Y. Qiu, Y. Wu, X. Wei, X. Luo, W. Jiang, L. Zheng, W. Gu, C. Zhu and Y. Yamauchi, Improvement in ORR Durability of Fe Single-Atom Carbon Catalysts Hybridized with CeO_2 Nanozyme, *Nano Letters*, 2024, 24, 9034-9041.

28. X. Cheng, X. Jiang, S. Yin, L. Ji, Y. Yan, G. Li, R. Huang, C. Wang, H. Liao, Y. Jiang and S. Sun, Instantaneous Free Radical Scavenging by CeO_2 Nanoparticles Adjacent to the Fe−N_4 Active Sites for Durable Fuel Cells, *Angewandte Chemie*, 2023, 135.

29. Y. Zhang, F. He, Y. Gao, X. Cui, S. Song, L. Cao, Z. Liu, Q. Sun, X. Zhang and P. Yang, CeO_2 Boosted Fe-N_5 Electrocatalyst via Relay Catalysis for Modulating Oxygen Reduction Reaction in Al-Air

Batteries, *Advanced Functional Materials*, 2025, https://doi.org/10.1002/adfm.202501806.

30. F. Nasim, H. Ali, A. Waseem and M. A. Nadeem, Investigating the effect of CeO_2 on the radical scavenging activity of Pt@ CoO_x/NC@CeO_2 during the electrocatalytic oxygen reduction reaction in acidic and alkaline environments, *Materials Advances*, 2024.

31. Z. Su, H. Wei, L. Zhang, H. Li, P. Liu, Z. Hou and X. Gong, Mesoporous and dual-shelled hollow CeO_2@CoNC nanospheres as efficient and stable oxygen reduction reaction electrocatalysts, *Electrochimica Acta*, 2023, 468.

32. H. Su, W. Gao, L. Li, H. Yuan and D. Wen, Oxygen Vacancy-Rich CeO_2 Quantum Dots Boost the Activity and Durability of Pt/C for Methanol Oxidation and Oxygen Reduction Reactions, *ACS Sustainable Chemistry & Engineering*, 2023, 11.

33. S. Kim and Y. J. Sa, Ce^{4+}/Ce^{3+} Redox-Promoted Electron Transfer for Efficient Neutral H_2O_2 Electrosynthesis from Two-Electron Oxygen Reduction, *ACS Catalysis*, 2024, https://doi.org/10.1021/acscatal.4c00625.

34. X. Mei, X. Zhao, Y. Chen, B. Deng, Q. Geng, Y. Cao, Y. Li and F. Dong, Highly Efficient H_2O_2 Production via Two-Electron Electrochemical Oxygen Reduction over Fe-Doped CeO_2, *ACS Sustainable Chemistry & Engineering*, 2023, 11.

35. M. Cheng, Z. Li, T. Xu, Y. Mao, Y. Zhang, G. Zhang and Z. Yan, Efficient overall $2e^-$ oxygen electrolysis to H_2O_2 on CeO_2 nanocubes, *Electrochimica Acta*, 2022, 430, 141091.

36. A. Sivanantham, P. Ganesan and S. Shanmugam, A synergistic effect of Co and CeO_2 in nitrogen-doped carbon nanostructure for the enhanced oxygen electrode activity and stability, *Applied Catalysis B: Environmental*, 2018, 237.

37. V. N. Kale and T. Maiyalagan, Interface Engineering of ZIF-67 derived Heterostructured CeO_2@Co_3O_4 Polyhedron Promoted by Reduced Graphene Oxide for Enhanced Oxygen Evolution Reaction, *Journal of Alloys and Compounds*, 2023, 961.

38. T. Montini, M. Melchionna, M. Monai and P. Fornasiero, Fundamentals and Catalytic Applications of CeO_2-Based Materials, *Chemical Reviews*, 2016, 116, 5987-6041.

39. E. Grulke, K. Reed, M. Beck, X. Huang, A. Cormack and S. Seal, Nanoceria: factors affecting its pro- and anti-oxidant properties, *Environmental Science Nano*, 2014, 1, 429-444.

40. J. Li, Y. Wang, X. Lu, K. Guo and C. Xu, Increased Oxygen Vacancies in CeO_2 for Improved Electrocatalytic Nitrogen Reduction Performance, *Inorganic Chemistry*, 2022, 61, 17242-17247.

41. M. Kumar, J.-H. Yun, V. Bhatt, B. Singh, J. Kim, J.-S. Kim, B. S. Kim and C. Y. Lee, Role of Ce^{3+} valence state and surface oxygen vacancies on enhanced electrochemical performance of single step solvothermally synthesized CeO_2 nanoparticles, *Electrochimica Acta*, 2018, 284, 709-720.

42. M. Melchionna, M. Bevilacqua and P. Fornasiero, The electrifying effects of carbon-CeO_2 interfaces in (electro)catalysis, *Materials Today Advances*, 2020, 6, 100050.

43. C. Pereira, D. M. Fernandes, A. F. Peixoto, M. Nunes, B. Jarrais, I. Kuźniarska-Biernacka and C. Freire, in *Catalysis for a Sustainable Environment: Reactions, Processes and Applied Technologies*, 2024, https://doi.org/10.1002/9781119870647.ch13.

44. Q. Li, L. Song, Z. Liang, M. Sun, T. Wu, B. Huang, F. Luo, Y. Du and C.-H. Yan, A Review on CeO_2-Based Electrocatalyst and Photocatalyst in Energy Conversion, *Advanced Energy and Sustainability Research*, 2021, 2, 2000063.

45. F. Zhang, R. Ke, M. Liu, X. Zhang, Y. Wang and Y. Wang, Improved electrocatalytic performance of Fe/CeO_2 bifunctional electrocatalyst by simultaneous H_2O_2 in-situ generation and activation, *Chemical Engineering Journal Advances*, 2022, 9, 100231.

46. B. Li, F. Wang, K. Li, P. Ning, M. Chen and C. Zhang, CeO_2-supported Fe, Co and Ni toward CO_2 hydrogenation: Tuning catalytic performance via metal-support interaction, *Journal of Rare Earths*, 2023, 41, 926-932.

47. X.-C. Sun, K. Yuan, W.-D. Hua, Z.-R. Gao, Q. Zhang, C.-Y. Yuan, H.-C. Liu and Y.-W. Zhang, Weakening the Metal–Support Interactions of M/CeO_2 (M = Co, Fe, Ni) Using a NH_3-Treated CeO_2 Support for an Enhanced Water–Gas Shift Reaction, *ACS Catalysis*, 2022, 12, 11942-11954.

48. Y. Yu, L. Gao, X. Liu, Y. Wang and S. Xing, Enhancing the Catalytic Activity of Zeolitic Imidazolate Framework-8-Derived N-Doped Carbon with Incorporated CeO_2 Nanoparticles in the Oxygen Reduction Reaction, *Chemistry – A European Journal*, 2017, 23, 10690-10697.

49. Y. Kang, W. Wang, J. Li, Y. Mi, H. Gong and Z. Lei, 3D Rosa centifolia-like CeO_2 encapsulated with N-doped carbon as an enhanced electrocatalyst for Zn-air batteries, *Journal of Colloid and Interface Science*, 2020, 578.

50. Y. Hao, L. Ge and S. H. Chan, ZIF-8 derived CeO_2-Fe_3O_4@Fe-N/C catalyst for oxygen reduction reaction, *Fuel Cells*, 2022, 22.

51. S. Wang, L. Li, Y. Zheng, C. Xu, Z. Zhuang, K. Sun, W. Yan and J. Zhang, Charge regulation through rare earth metal oxides for single-atomic/cluster Co-based electrocatalysts towards boosting oxygen reduction reaction, *Applied Catalysis B: Environment and Energy*, 2025, 377, 125493.

52. L. Chen, P. Fleming, V. Morris, J. D. Holmes and M. A. Morris, Size-Related Lattice Parameter Changes and Surface Defects

in Ceria Nanocrystals, *Journal of Physical Chemistry C*, 2010, 114, 12909-12919.

53. D. Prieur, W. Bonani, K. Popa, O. Walter, K. W. Kriegsman, M. H. Engelhard, X. Guo, R. Eloirdi, T. Gouder and A. Beck, Size dependence of lattice parameter and electronic structure in CeO_2 nanoparticles, *Inorganic Chemistry*, 2020, 59, 5760-5767.

54. J. Paier, C. Penschke and J. Sauer, Oxygen Defects and Surface Chemistry of Ceria: Quantum Chemical Studies Compared to Experiment, *Chemical Reviews*, 2013, 113.

55. S. Luo, M. Li, V. Fung, B. G. Sumpter, J. Liu, Z. Wu and K. Page, New insights into the bulk and surface defect structures of ceria nanocrystals from neutron scattering study, *Chemistry of Materials*, 2021, 33, 3959-3970.

56. Y. Sun, T. Wu, Z. Bao, J. Moon, Z. Huang, Z. Chen, H. Chen, M. Li, Z. Yang and M. Chi, Defect engineering of ceria nanocrystals for enhanced catalysis via a high-entropy oxide strategy, *ACS Central Science*, 2022, 8, 1081-1090.

57. I. d. C. Silva, F. A. Sigoli and I. O. Mazali, Reversible Oxygen Vacancy Generation on Pure CeO_2 Nanorods Evaluated by in Situ Raman Spectroscopy, *The Journal of Physical Chemistry C*, 2017, 121.

58. M. Mogensen, N. M. Sammes and G. A. Tompsett, Physical, chemical and electrochemical properties of pure and doped ceria, *Solid State Ionics*, 2000, 129.

59. R. Schmitt, A. Nenning, O. Kraynis, R. Korobko, A. I. Frenkel, I. Lubomirsky, S. M. Haile and J. L. Rupp, A review of defect structure and chemistry in ceria and its solid solutions, *Chemical Society Reviews*, 2020, 49, 554-592.

60. S. Loridant, Raman spectroscopy as a powerful tool to characterize ceria-based catalysts, *Catalysis Today*, 2021, 373.

61. H. Li, P. Zhang, G. Li, J. Lu, Q. Wu and Y. Gu, Stress measurement for nonstoichiometric ceria films based on Raman spectroscopy, *Journal of Alloys and Compounds*, 2016, 682, 132-137.

62. Y. Zheng, K. Fu, Z. Yu, Y. Su, R. Han and Q. Liu, Oxygen vacancies in a catalyst for VOCs oxidation: synthesis, characterization, and catalytic effects, *Journal of Materials Chemistry A*, 2022, 10, 14171-14186.

63. Z. Wu, M. Li, J. Howe, H. M. Meyer III and S. H. Overbury, Probing defect sites on CeO_2 nanocrystals with well-defined surface planes by Raman spectroscopy and O_2 adsorption, *Langmuir*, 2010, 26, 16595-16606.

64. A. Martínez-Arias, J. C. Conesa and J. Soria, O_2-probe EPR as a method for characterization of surface oxygen vacancies in ceria-based catalysts, *Research on Chemical Intermediates*, 2007, 33, 775-791.

65. R. M. Rakhmatullin, V. V. Semashko, S. L. Korableva, A. G. Kiiamov, A. A. Rodionov, R. Tschaggelar, J. A. van Bokhoven and C. Paun, EPR study of ceria nanoparticles containing different concentration of Ce^{3+} ions, *Materials Chemistry and Physics*, 2018, 219, 251-257.

66. S. Gadipelli and Z. X. Guo, Tuning of ZIF-derived carbon with high activity, nitrogen functionality, and yield – a case for superior CO_2 capture, *ChemSusChem*, 2015, 8, 2123-2132.

67. W. Alnoush, N. Noor, A. Abdellah, S. Tan, S. Angizi and D. Higgins, Mitigating Cobalt Nanoparticles in Pyrolyzed Co-ZIF-Derived Oxygen Reduction Reaction Electrocatalysts in Alkaline Media, *Applied Catalysis B: Environment and Energy*, 2025, https://doi.org/10.1016/j.apcatb.2025.126121126121.

68. Y. Zhou, X. Deng, H. Xing, H. Zhao, Y. Liu, L. Guo, J. Feng, W. Feng, Y. Zong and X. Zhu, Dynamically observing the formation of MOFs-driven Co/N-doped carbon nanocomposites by in-situ transmission electron microscope and their application as high-efficient microwave absorbent, *Nano Research*, 2022, 15, 6819-6830.

69. N. Cui, K. Bi, W. Sun, Q. Wu, Y. Li, T. Xu, B. Lv and S. Zhang, Effect of pyrolysis conditions on the performance of Co–doped MOF–derived carbon catalysts for oxygen reduction reaction, *Catalysts*, 2021, 11, 1163.

70. W. Peng, X. Yang, L. Mao, J. Jin, S. Yang, J. Zhang and G. Li, ZIF-67-derived Co nanoparticles anchored in N doped hollow carbon nanofibers as bifunctional oxygen electrocatalysts, *Chemical Engineering Journal*, 2021, 407, 127157.

71. X. Zhang, J. Lin, S. Chen, J. Yang, L. Song, X. Wu and H. Xu, Co Nanoparticles Encapsulated in N-Doped Carbon Nanosheets: Enhancing Oxygen Reduction Catalysis without Metal–Nitrogen Bonding, *ACS Applied Materials & Interfaces*, 2017, 9, 38499-38506.

72. Z.-K. Han, W. Liu and Y. Gao, Advancing the Understanding of Oxygen Vacancies in Ceria: Insights into Their Formation, Behavior, and Catalytic Roles, *JACS Au*, 2025, 5, 1549-1569.

73. G. N. Vayssilov, Y. Lykhach, A. Migani, T. Staudt, G. P. Petrova, N. Tsud, T. Skála, A. Bruix, F. Illas and K. C. Prince, Support nanostructure boosts oxygen transfer to catalytically active platinum nanoparticles, *Nature materials*, 2011, 10, 310-315.

74. Y. Lykhach, S. M. Kozlov, T. Skála, A. Tovt, V. Stetsovych, N. Tsud, F. Dvořák, V. Johánek, A. Neitzel and J. Mysliveček, Counting electrons on supported nanoparticles, *Nature materials*, 2016, 15, 284-288.

75. S. G. Peera and S. W. Kim, Rare Earth Ce/CeO_2 Electrocatalysts: Role of High Electronic Spin State of Ce and Ce^{3+}/Ce^{4+} Redox Couple on Oxygen Reduction Reaction, *Nanomaterials*, 2025, 15, 600.

76. W. Yuan, J. Li, H. Yang, Z. Chen, Z. Liu, H. Huang, Y. Liu and Z. Kang, Enhanced electron transfer kinetics via constructing co-

View Article Online
DOI: 10.1039/D6TA01057A

catalytic system of cerium oxide and carbon dots enabling efficient electrosynthesis of hydrogen peroxide in neutral media, *Journal of Electroanalytical Chemistry*, 2024, 971.

77. H. Luo, J. Wang, S. Zhang, B. Sun, Z. Chen, X. Ren, Z. Luo, X. Han and W. Hu, In Situ Symbiosis of Cerium Oxide Nanophase for Enhancing the Oxygen Electrocatalysis Performance of Single-Atom Fe─N─C Catalyst with Prolonged Stability for Zinc–Air Batteries, *Small*, 2024, https://doi.org/10.1002/smll.202400357.

78. F.-D. Tu, Z.-Y. Wu, P. Guo, L.-X. Shen, Z.-Y. Zhang, Y.-K. Dai, M. Ma, J. Liu, B. Xu, Y.-L. Zhang, L. Zhao and Z.-B. Wang, Fe-N-C catalysts decorated with oxygen vacancies-rich CeO_x to increase oxygen reduction performance for Zn-air batteries, *Journal of Colloid and Interface Science*, 2023, 637.

79. X. Hai, S. Xi, S. Mitchell, K. Harrath, H. Xu, D. F. Akl, D. Kong, J. Li, Z. Li, T. Sun, H. Yang, Y. Cui, C. Su, X. Zhao, J. Li, J. Pérez-Ramírez and J. Lu, Scalable two-step annealing method for preparing ultra-high-density single-atom catalyst libraries, *Nature Nanotechnology*, 2022, 17, 174-181.

80. S. Chen, T. Luo, X. Li, K. Chen, J. Fu, K. Liu, C. Cai, Q. Wang, H. Li, Y. Chen, C. Ma, L. Zhu, Y.-R. Lu, T.-S. Chan, M. Zhu, E. Cortés and M. Liu, Identification of the highly active Co–N_4 Coordination motif for selective oxygen reduction to hydrogen peroxide, *Journal of the American Chemical Society*, 2022, 144, 14505-14516.

View Article Online
DOI: 10.1039/D6TA01057A

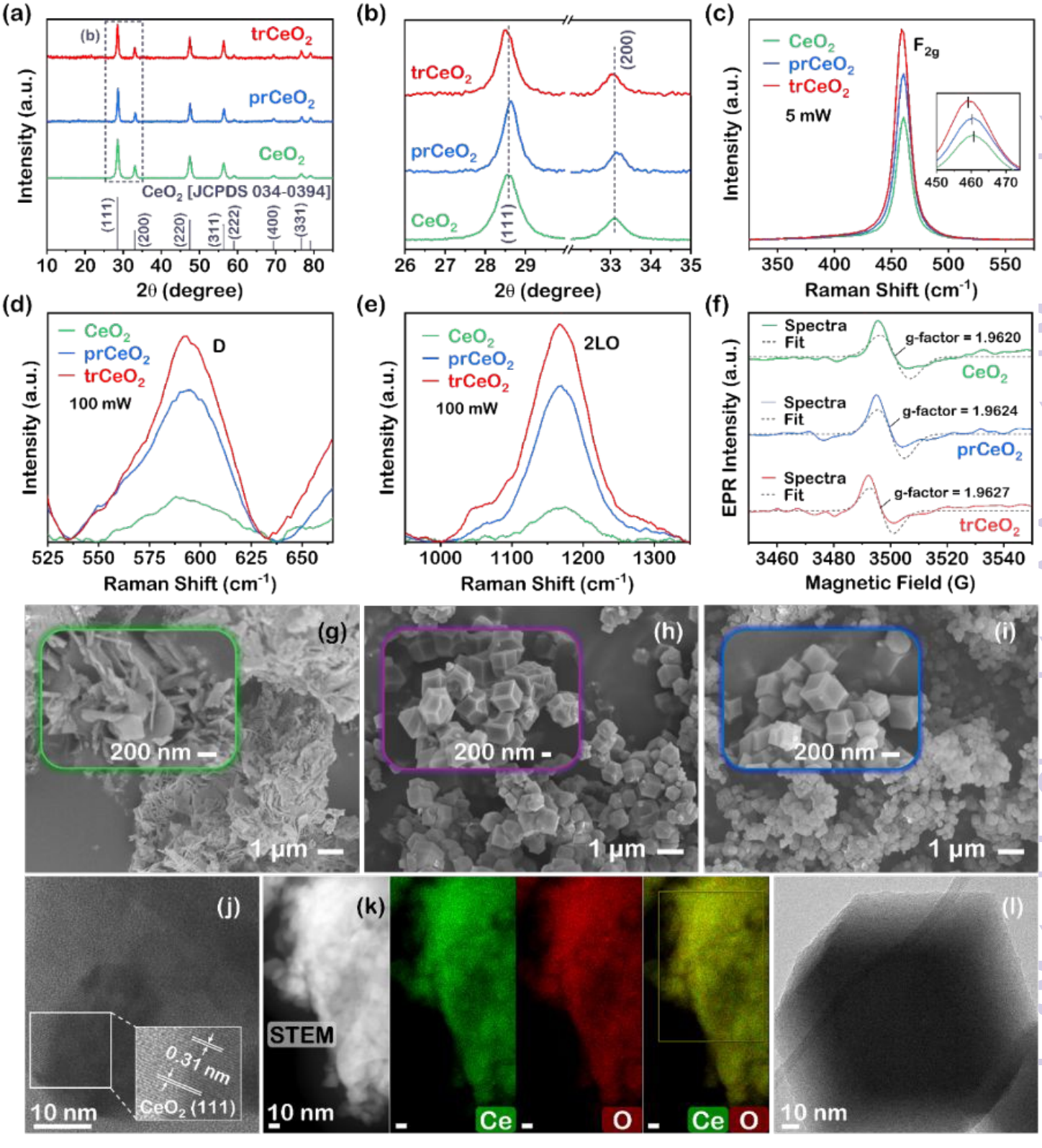

Figure 1 Structural characterization of precursors. (a) XRD patterns of CeO_2, $prCeO_2$, and $trCeO_2$ with a fluorite ceria reference. (b) Enlarged XRD region (26°-35° 2θ) highlighting shifts in the (111) and (200) peaks. (c-e) Raman F_{2g}, D, and 2LO bands of CeO_2, $prCeO_2$, and $trCeO_2$. (f) EPR spectra of CeO_2, $prCeO_2$, and $trCeO_2$. SEM images of (g) CeO_2, (h) CeO_2@Zn-ZIF8, and (i) CeO_2@Co/Zn-ZIF. (j) HR-TEM of CeO_2 with a measured d-spacing of 0.31 nm corresponding to the (111) plane. (k) STEM-EELS mapping of CeO_2. (l) TEM of a Zn-ZIF8 particle.

View Article Online
DOI: 10.1039/D6TA01057A

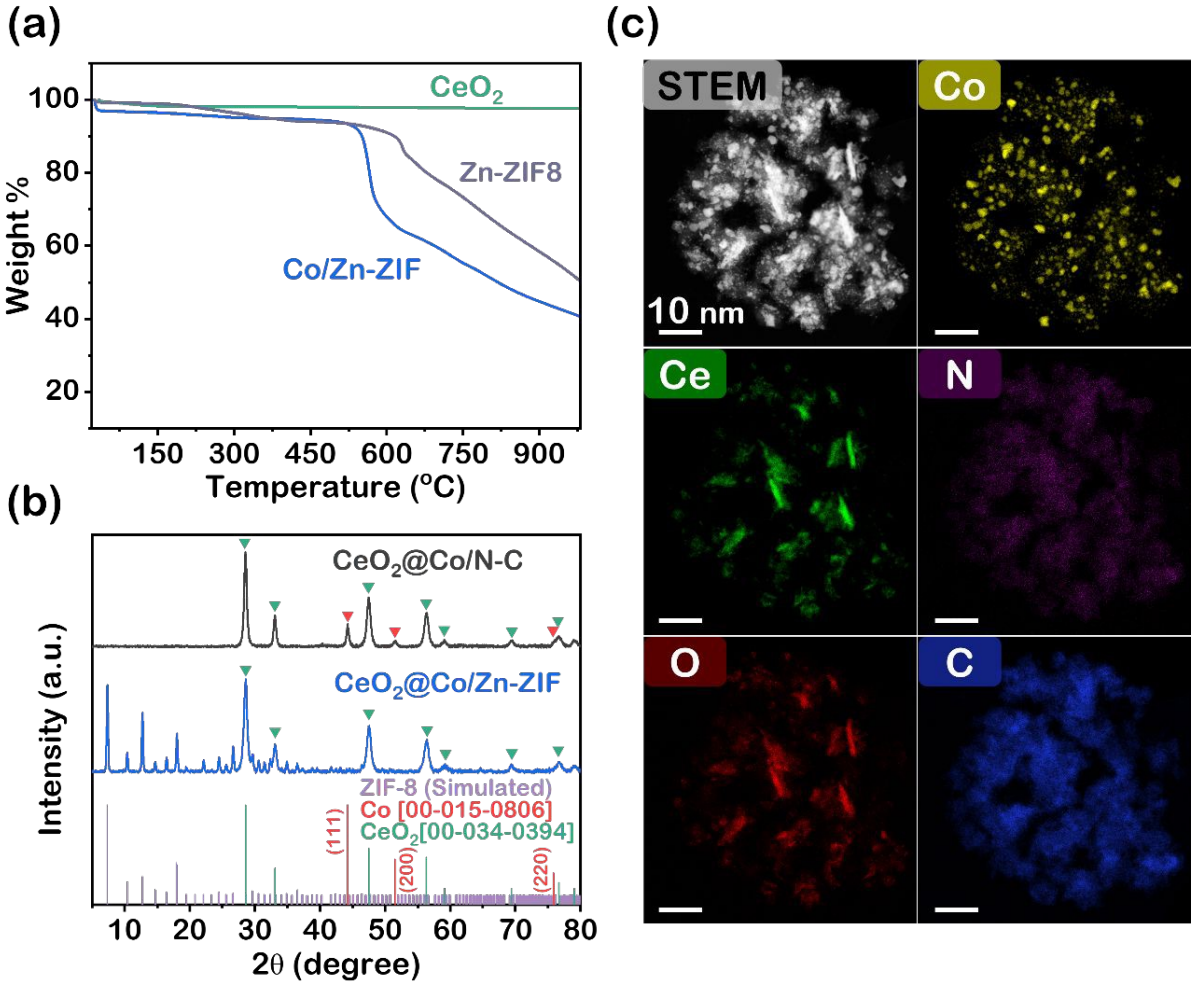

Figure 2 Thermal transformation and post-pyrolysis characterization. (a) TGA of CeO_2, Zn-ZIF8, and Co/Zn-ZIF precursor components in the temperature range of 25-1000 °C. (b) XRD diffraction patterns of the pre-pyrolysis CeO_2@CoZn-ZIF precursor and the post-pyrolysis CeO_2@Co/N-C electrocatalyst. (c) STEM-EDX elemental mapping of the CeO_2@Co/N-C electrocatalyst.

View Article Online
DOI: 10.1039/D6TA01057A

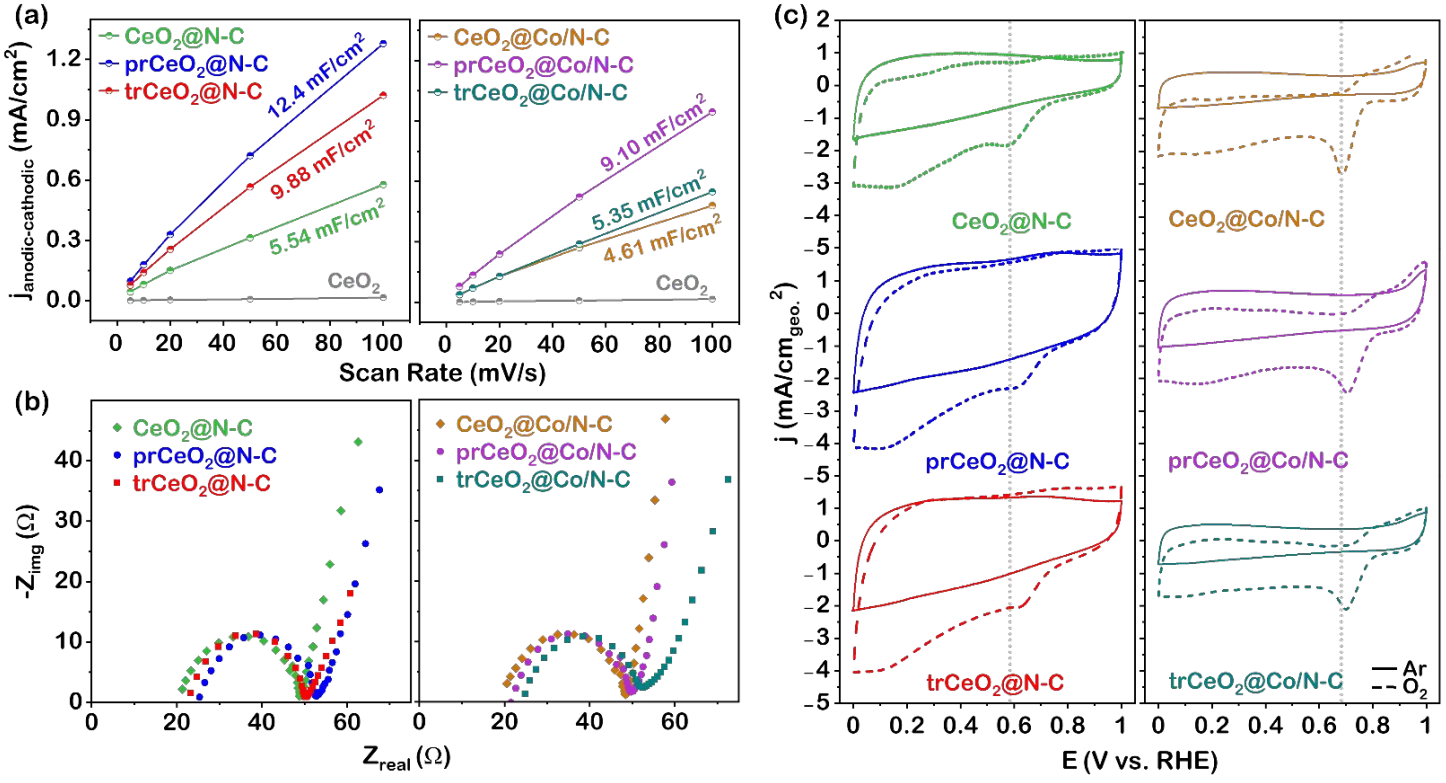

Figure 3 Electrochemical characterization of ceria@N-C and ceria@Co/N-C electrocatalysts. (a) The difference between anodic and cathodic current densities versus scan rate for C_{dl} determination. (b) EIS Nyquist plots. (c) CVs under Ar- and O_2-saturated 0.1 M KOH.

View Article Online
DOI: 10.1039/D6TA01057A

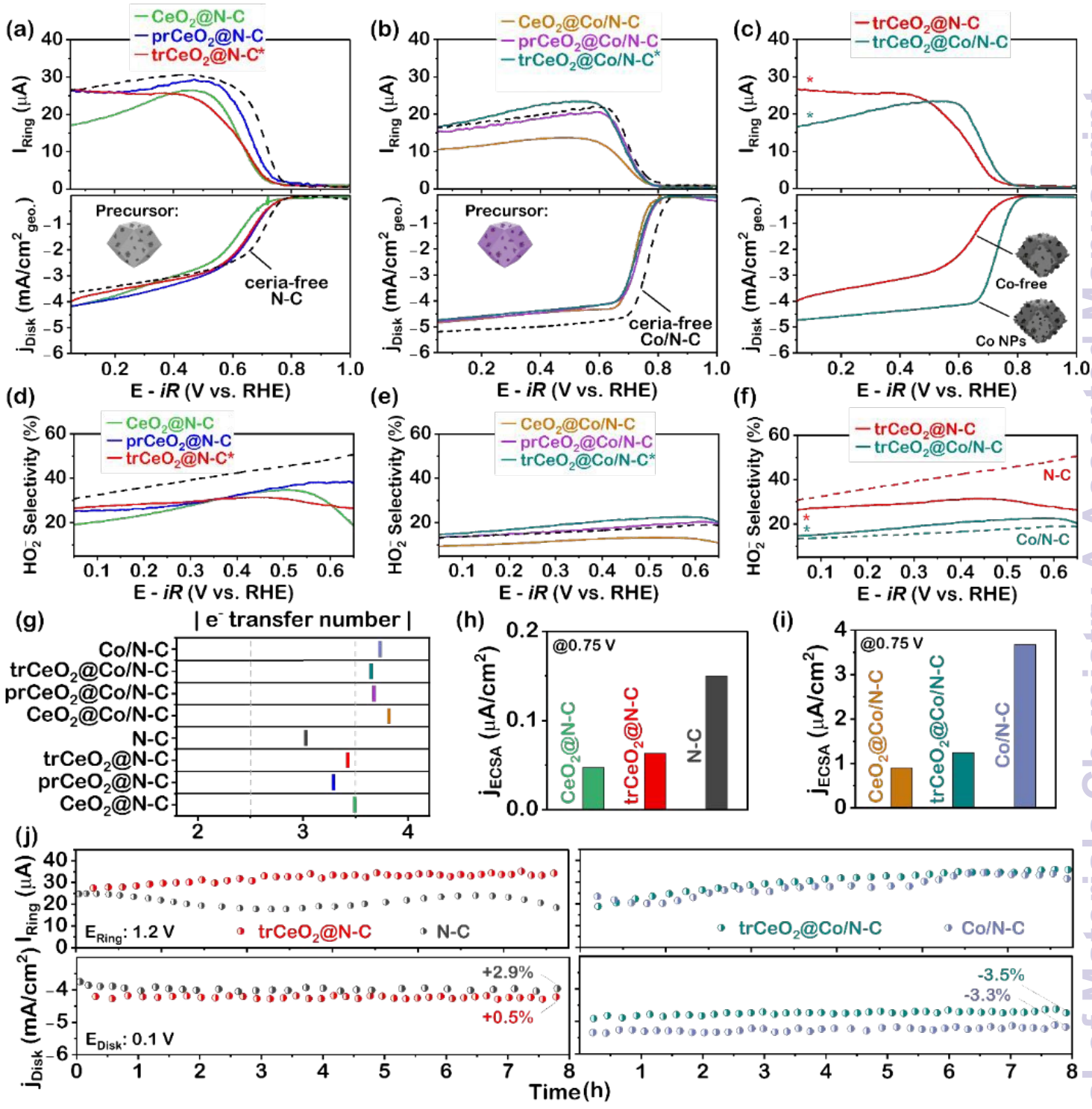

Figure 4 Electrochemical ORR performance evaluation in 0.1 M KOH. ORR polarization curves at 1600 rpm of (a) ceria@N-C electrocatalysts (CeO_2@N-C, $prCeO_2$@N-C, and $trCeO_2$@N-C), (b) ceria@Co/N-C electrocatalysts (CeO_2@Co/N-C, $prCeO_2$@Co/N-C, and $trCeO_2$@Co/N-C), and (c) $trCeO_2$-embedded electrocatalysts ($trCeO_2$@N-C and $trCeO_2$@Co/N-C). HO_2^- selectivity of (d) ceria@N-C electrocatalysts, (e) ceria@Co/N-C electrocatalysts, and (f) $trCeO_2$-embdedded electrocatalysts. (g) Average electron transfer number for all electrocatalysts. (h) Specific activity comparison of CeO_2@N-C, $trCeO_2$@N-C, and N-C. (i) Specific activity comparison of CeO_2@Co/N-C, $trCeO_2$@Co/N-C, and Co/N-C. RRDE chronoamperometry test at 0.1 V vs. RHE of $trCeO_2$@N-C, N-C, $trCeO_2$@Co/N-C, and Co/N-C.

View Article Online
DOI: 10.1039/D6TA01057A

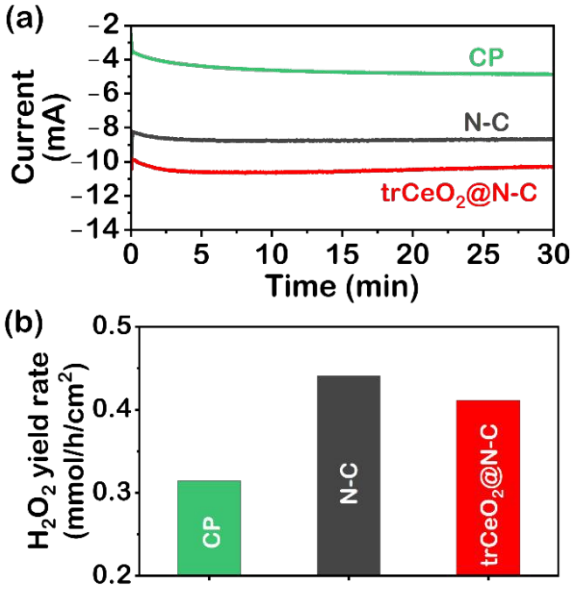

Figure 5 Electrochemical testing in two-compartment H-cell at 0.1 V vs. RHE for H_2O_2 yield rate quantification. (a) 30-minute chronoamperometric response of carbon paper, N-C, and $trCeO_2$@N-C. (b) H_2O_2 yield rate of carbon paper, N-C, and $trCeO_2$@N-C.

View Article Online
DOI: 10.1039/D6TA01057A

Data will be made available from the corresponding author upon reasonable request. Supplementary information is available and includes: calculation details for XRD, EPR, ECSA, and RRDE analyses, EIS circuit modeling, ring collection efficiency calibration, supplementary characterization figures (XRD, Raman, EPR, SEM, STEM-EELS), and supplementary tables. See DOI: [DOI_HERE]